in animal experiments. As type III collagen is closely associated with the appearance of macrophages and metalloproteinase, high frequency ultrasound possibly detect a vulnerable plaque leading to coronary syndrome. Development of high frequency technologies in informative technologies and micro- and nano-machine techniques would contribute the development of high frequency ultrasound imaging also in clinical settings.

Cells are considered as a visco-elastic material and the acoustic microscopy shows information on viscosity by attenuation and information on elasticity by sound speed. In stead of stretching cells or using atomic force microscopy for measuring biomechanical properties, acoustic microscopy can be used to measure precise mechanical property distribution without contact.

5. References

[SOK 49] SOKOLOV S (1949) The ultrasonic microscope. *Doklady. Akademi.i Nauk. SSSR. 64:* 333-335.

[DUN 59] DUNN F, FRY WJ (1959) Ultrasonic absorption microscope. *J. Acoust. Soc. Am. 31:* 632-633.

[LEM 73] LEMONS RA, QUATE CF (1973) A scanning acoustic microscope. *Proc IEEE Ultrason. Symp.*18-20.

[KUS 85] KUSHIBIKI J, CHUBACHI N. (1985) Material characterization by line-focused-beam acoustic microscope. *IEEE. Trans. Sonics. Ultrason. SU-32:* 132-135.

[OKA 85] OKAWAI H, TANAKA M, CHUBACHI N, KUSHIBIKI J (1985) Non-contact simultaneous measurement of thickness and acoustic properties of a biological tissue using focused wave in a scanning acoustic microscope. *Jpn. J. Appl. Phys. 26:*52-54.

[BAR 91] BARR RJ, WHITE GM, JONES JP, SHAW LB, ROSS PA (1991) Scanning acoustic microscopy of neoplastic and inflammatory cutaneous tissue specimens. *J. Invest. Dermatol. 96:* 38-42.

[JON 96] JONES JP (1996) Applications of acoustical microscopy in dermatology. *Ultrasonic Tissue Characterization, Springer-Verlag:* 201-212.

[SAI 91] SAIJO Y, TANAKA M, OKAWAI H, DUNN F (1991) The ultrasonic properties of gastric cancer tissues obtained with a scanning acoustic microscope system. *Ultrasound in Med. and Biol. 17:* 709-714.

[SAS 96] SASAKI H, SAIJO Y, TANAKA M, OKAWAI H, TERASAWA Y, YAMBE T, NITTA S (1996) Influence of tissue preparation on the high-

frequency acoustic properties of normal kidney tissue. *Ultrasound in Med. and Biol. 22:* 1261-1265.

[SAI 97] SAIJO Y, TANAKA M, OKAWAI H, SASAKI H, NITTA S, DUNN F (1997) Ultrasonic tissue characterization of infarcted myocardium by scanning acoustic microscopy. *Ultrasound in Med. and Biol. 23:* 77-85.

[CHA 97] CHANDRARATNA PAN, WHITTAKER P, CHANDRARATNA PM, GALLET J, KLONER RA, HLA A (1997) Characterization of collagen by high-frequency ultrasound: Evidence for different acoustic properties based on collagen fiber morphologic characteristics. *Am. Heart J. 133:* 364-368.

[SAI 05] SAIJO Y, SASAKI H, HOZUMI N, KOBAYASHI K, TANAKA M, YAMBE T (2005) Sound speed scanning acoustic microscopy for biomedical applications. *Technol Health Care. 13*: 261-267.

[SAI 98] SAIJO Y, SASAKI H, OKAWAI H, NITTA S, TANAKA M (1998) Acoustic properties of atherosclerosis of human aorta obtained with high-frequency ultrasound. *Ultrasound Med Biol. 24:* 1061-1064.

[SAI 01] SAIJO Y, JORGENSEN CS, FALK E (2001) Ultrasonic tissue characterization of collagen in lipid-rich plaques in apoE-deficient mice. Atherosclerosis 158; 289-295.

EuroIntervention

IVUS beyond the horizon

Antonius F.W. van der Steen[1,2]*, Radj A. Baldewsing[1], F. Levent Degertekin[3], Stanislav Emelianov[4], Martijn. E. Frijlink[1], Yuji Furukawa[5], Dave Goertz[1,2], Mustafa Karaman[6], Pierre T. Khuri-Yakub[7], Kang Kim[8], Frits Mastik[1], T. Moriya[9], Ömer Oralkan[7], Yoshifumi Saijo[10], Johannes A Schaar[1], Patrick W Serruys[1], Shriram Sethuraman[4], Akira Tanaka[11], Hendrik. J. Vos[1,12], Russell Witte[8], Matthew O'Donnell[8]

1. Biomedical Engineering, Thorax Center Erasmus MC, Rotterdam, The Netherlands; 2. Interuniversity Cardiology Institute of the Netherlands; 3. Georgia Institute of Technology, Atlanta, Georgia, USA; 4. Department of Biomedical Engineering, The University of Texas at Austin, USA; 5. Tokyo University of Agriculture and Technology, Tokyo, Japan; 6. Isik University, Istanbul, Turkey; 7. E. L. Ginzton Laboratory, Stanford University, Stanford, California, USA; 8. Department of Biomedical Engineering, Univ. of Michigan, Ann Arbor, USA; 9. Tokyo Metropolitan University, Tokyo, Japan; 10. Institute of Development, Aging and Cancer, Tohoku University, Sendai, Japan; 11. Faculty of Symbiotic Systems Science, Fukushima University, Fukushima, Japan; 12. Seismics and acoustics, Technical University Delft, The Netherlands

Introduction

Intravascular Ultrasound is a clinically available technique that can image the vessel wall and atherosclerotic plaque[1]. Although the first patent on this technique dates from 1972[2,3], the first catheters for clinical use were only available in the late eighties[4,5]. Since then this diagnostic technique is ever evolving. The main clinical applications to date have been assessment of free lumen and atherosclerotic plaque area[6], volume and therapy guidance[7,8] and guidance of stent placement[9]. To a lesser extent, it has been used for dosimetry in brachytherapy[10] and for assessing the true 3D orientation of coronary arteries and plaque to perform haemodynamic and shear stress studies[11-13].

At present, IVUS has only been used to a limited percentage of its potential. Most concepts mature outside the view of a clinical audience, but are widely discussed in the technical ultrasonics and biomedical engineering societies before they become available products. Probably the most appropriate platform for this has been the annually held IEEE Ultrasonics Symposium. Most IVUS equipment and signal processing methods were discussed here long before they became available in the clinic[14,15]. The array catheter and its beam forming were introduced in 1991[16]. Also forward looking IVUS has been discussed by several groups[17,18]. Qualitative flow[19,20] and quantitative flow[21-23] assessment derived from IVUS data were introduced here as well as tissue characterization using RF data, now available under the name Virtual Histology[24-27]. Also IVUS Elastography, Palpography and tissue velocity imaging[28-32] were nurtured at this symposium.

This paper gives a review of IVUS techniques under development that were discussed at the 2005 IEEE Ultrasonics symposium. Although not all will become products, it gives a good impression of what is cooking in engineering kitchens.

Forward-Viewing IVUS using CMUTs

Forward-viewing ultrasound volume images are desired for many intravascular and intracardiac applications such as guiding treatment of chronic total occlusion, helping stent deployment, and monitoring ablation procedures in the heart. Because of the requirements for a guidewire in catheters, an annular ring is the preferred geometry for transducer arrays. However, it is very challenging to implement this geometry in a very small scale (1-2 mm) using existing piezoelectric transducer technology[18].

* *Corresponding author: Biomedical Engineering, Thorax Center Ee 23.02, Erasmus MC Rotterdam, P.O. Box 1738, 3000 DR Rotterdam, The Netherlands*

E-mail: a.vandersteen@erasmusmc.nl

Capacitive Micro-machined Ultrasonic Transducers (CMUT) are transducers that consist of many tiny air filled capacitors, with a flexible electrode membrane on top. When a DC bias voltage is applied to these miniature membrane transducers a stress is developed proportional to the voltage applied squared and the top electrode membrane deflects. Operationally they show a lot of similarity to piezoelectric materials, but they do have a few distinct advantages.

CMUT arrays can be made in any arbitrary geometry with very small dimensions using photo-lithographic techniques and standard micro-fabrication processes. In addition to their ease of fabrication, CMUTs also offer performance advantages such as wide bandwidth and improved sensitivity[33]. CMUTs are also particularly suited for high frequency arrays because the fabrication process used is routinely able to produce features several microns in size. Recent developments in micro-machined ultrasound transducer technology have enabled implementation of IVUS arrays for forward-looking imaging at the tip of a catheter[17,34]. This technology is currently implemented by a group from Stanford[35] and a group from Georgia Tech[36].

At Stanford, a 64-element, 2-mm diameter CMUT ring array allows full synthetic phased array volumetric images to be generated with integrated electronics (Figure 1a).

At Georgia Institute of Technology, a similar array with a 1.15 mm diameter has been constructed[37-38]. (Figure 1bc)

An interesting feature of CMUT operation is the ability to change the operating frequency by changing the DC bias. If the DC bias is made so high that the upper membrane just touches the lower, the so called collapse mode, the membrane cannot vibrate any more at its fundamental resonance frequency and it will vibrate at harmonic frequencies. The resulting operating frequencies in conventional and collapse regimes for these arrays can be e.g. 8.5 MHz and 19 MHz, respectively. Potentially, this operating flexibility of CMUTs allows on-demand switching between its two modes of operation during the imaging procedure, thereby providing a choice between the low frequency conventional mode with high penetration for navigation and the high frequency collapse mode with high resolution for diagnosis. The imaging capacity of forward looking arrays is shown in Figure 2. Phantoms including deployed and undeployed forms of a Palmaz-Schatz coronary stent have been imaged.

It should be understood that such elements have not been mounted on a catheter yet. Minimization and integration of electronics are the main challenges in the near future.

Ultrasonic micromotor for IVUS

Commercially available IVUS catheters contain either 64 static elements or one rotating element. An advantage of a single element is that it is larger, and thus it is easier to obtain a good signal to noise ratio or achieve higher frequencies, resulting in a higher resolution. One of the disadvantages of a mechanically rotating IVUS systems is non-uniform rotational distortion (NURD)[31,39], caused by the long flex between the ultrasound element and the motor driving it. NURD can be overcome by rotating a transducer or a mirror using a micro motor placed close to them. The feasibility of an electromagnetic micromotor for IVUS has been shown in the past[40,41]. Given that metallic structures are potentially present in the close vicinity of the micromotor, including guidewires and stents, the design and manufacturing of an electromagnetic motor is quite critical. If the magnetic field is not fully contained in the motor, it may stop rotating or perform in an unpredictable fashion.

Ultrasonic motors do not suffer from this problem. In Tokyo, a new ultrasonic micromotor, 1 mm in diameter and 3 mm in length has been built[42]. It can work in a liquid environment and is hollow, so that electronic connection wires for the transducer can pass through. The ultrasonic motor uses a wave guide in the shape of a helical coil as a stator. The coiled stator is placed inside or outside of the rotor and the stator is pressed to the rotor. The motor operates as a travelling wave type ultrasonic motor, a flexural wave propagates along the coiled acoustic wave guide. This so called "lamb wave" crawls like a caterpillar over the rotor. Since the stator is fixed this makes the rotor rotate. Two operational realizations of the motor are illustrated in Figure 3. In Figure 3a, the stator is placed outside the rotor, the diameter is 1 millimetre. In Figure 3b, the stator is placed inside the rotor. This version needs to miniaturized further since is has at present a diameter of 2 millimetres. The rotor of the first one is capable of rotating with a speed of approximately 500 - 2,000 r.p.m, the second one at 5000-8000 r.p.m., both according to the ultrasonic power delivered. Another feature of the motor is that the transducer to excite the Lamb wave and the driving part consisting of the rotor and the stator are separated. Since the former can be placed outside the body, the driving part can be made as small as 0.8 mm in diameter and 3mm in length. Although the concept works, the technology still needs to be transferred to a catheter.

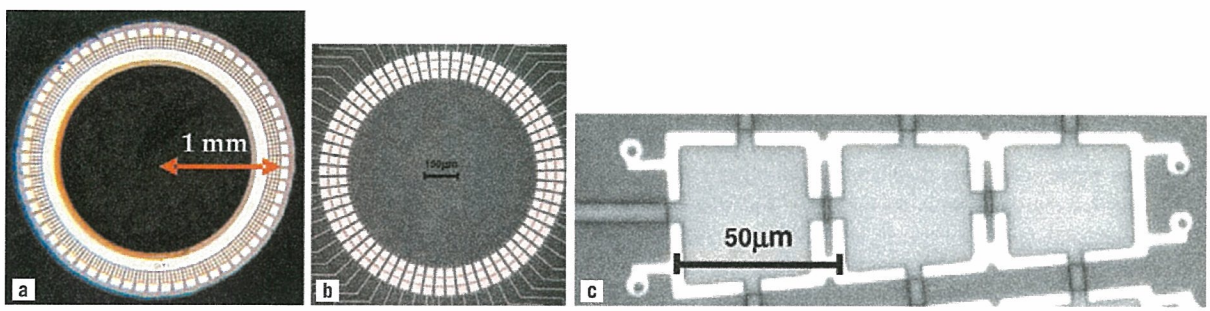

Figure 1. (a) Magnified view of the Stanford CMUT annular ring array. (b) Magnified view of the Georgia Tech CMUT annular ring array. (c) Further magnification of one element of the Georgia Tech array, each consists of f 3 rectangular cells connected in parallel.

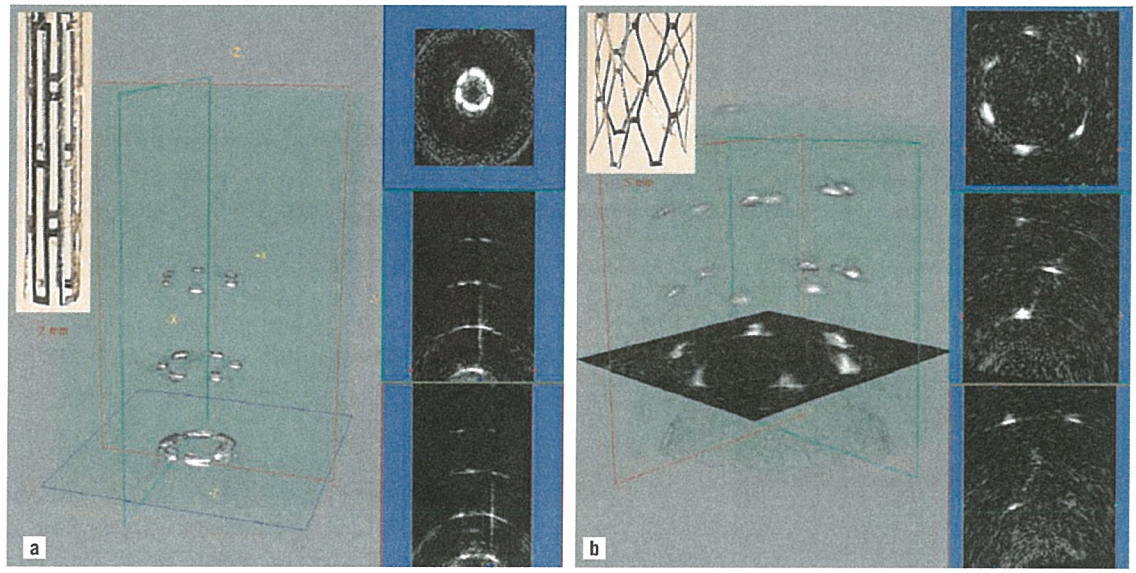

Figure 2. 3-D rendered ultrasound images and some cross-sections acquired with the Stanford array of (a) an undeployed Palmaz-Schatz stent; and (b) a deployed Palmaz-Schatz stent.

Harmonic IVUS

Since its introduction[43,44], Tissue Harmonic Imaging (THI) has increased the diagnostic value of conventional echocardiography. THI is a technique by which the received scattered ultrasound contains higher harmonics of the transmitted pulse due to non-linear sound propagation. THI enhances image quality through the combination of low harmonic content in the near field, a narrower beam, and reduced side lobe levels.

Although THI has been shown to increase image quality in medical ultrasound below 10 MHz, little work has been done to assess the benefits in IVUS applications. Initial studies showed the feasibility of THI at high frequencies for Ultrasound Biomicroscopy (UBM) and IVUS *in vitro*[45,46]. The reduction of stent imaging artifacts was shown when high frequency (20 - 40 MHz) THI was applied with a focused UBM transducer[47]. *In vivo* feasibility experiments of THI for an IVUS system using both a conventional and a custom-made mechanically-rotated IVUS catheter were described[48].

A prototype IVUS imaging system using a fast-rotating single element was constructed to do phantom experiments and perform *in vivo* imaging. To study the ability of a conventional IVUS catheter and a custom-made Harmonic IVUS catheter[49] to generate the required fundamental pressure to build up a detectable level of propagation harmonics, imaging experiments were performed. Data was acquired in fundamental 20 MHz (F20), harmonic 40 MHz (H40) mode, and for comparison purposes also in fundamental 40 MHz mode (F40). Harmonic images of cross-sections of an atherosclerotic aorta of a New Zealand White rabbit *in vivo* were formed by means of the Pulse Inversion (PI) technique. Signal-to-noise ratios (SNR) in H40 acquisitions were estimated *in vivo* for both catheters when driven by an F20 pulse with equal amplitude.

Cross-sectional images of the rabbit aorta *in vivo* were created using THI (Figure 4). The combined effect of amplifier saturation and reflections of the surrounding sheath, visible close to the transducer, is the least visible in H40 acquisition compared to both fundamental acquisitions. The latter emphasizes the advantage of reducing acoustic energy in the near field through the use of the harmonic beam. Recently, a transducer element (Figure 5) optimized for intravascular harmonic imaging, showing a frequency response

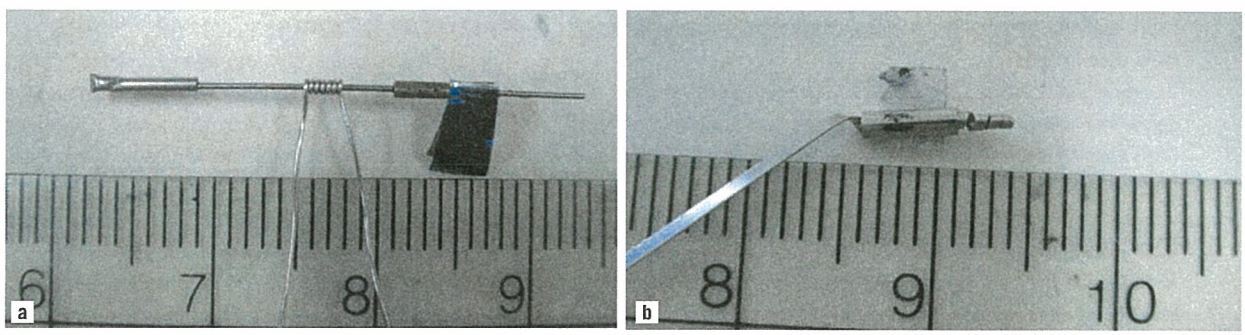

Figure 3. a. Ultrasound micromotor with an external stator. A flexural wave propagates along the coiled acoustic waveguide. This wave crawls like a caterpillar over the rotor, and makes it rotate. b. Ultrasound micromotor with an internal stator. (Scale is in cm)

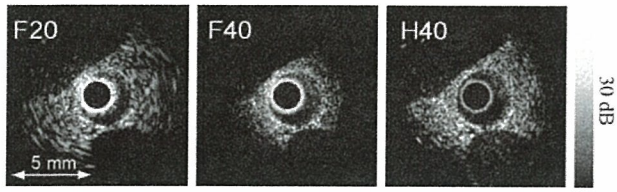

Figure 4. Cross-sections of an atherosclerotic rabbit aorta acquired in F20, F40 and H40 mode in vivo. These images are normalized with respect to the maximum signal level in the individual images.

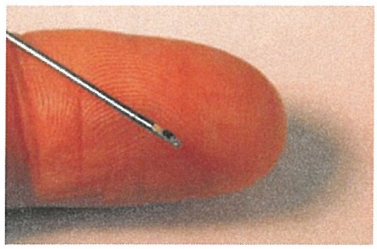

Figure 5a. The dual frequency transducer.

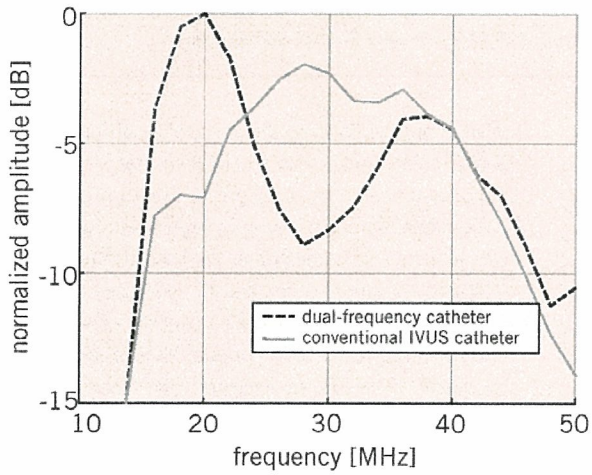

Figure 5b. One-way frequency responses of the dual-frequency catheter and a conventional IVUS catheter.

with two peaks around 20 and 40 MHz, has been designed, fabricated and characterized[49]. The main difference is an improved efficacy in transmit of 6 dB.

The *in vivo* imaging experiment resulted in a significant SNR improvement (>12 dB) in H40 mode of the custom-made catheter relative to the conventional catheter (Figure 6). However, careful interpretation is necessary since the aortas of only two different animals were imaged.

Incorporating optimised IVUS catheters for Harmonic Imaging indicates that instrumentation developments can improve harmonic IVUS imaging. Current studies investigate the feasibility of Harmonic IVUS with available clinical IVUS systems.

Contrast intravascular ultrasound

Microbubble contrast agents have been employed extensively at lower diagnostic ultrasound frequencies[50], but have seen little use in intravascular ultrasound. While microbubbles can in some circumstances be visualised through simple echogenicity enhancement, sensitive and specific detection of the agent is invariably

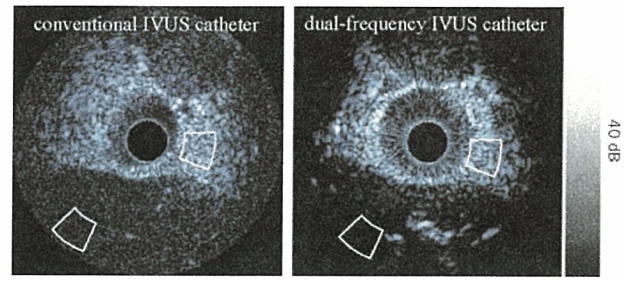

Figure 6. Cross-sections of rabbit aortas acquired in H40 mode with both a conventional and a dual-frequency IVUS catheter. Gray contours show the regions of interest for the SNR estimation.

achieved using more bubble-specific acoustic signatures. Two approaches employed successfully at lower frequencies are second harmonic imaging (listening at twice the ultrasound transmit frequency) and subharmonic imaging (listening at half the ultrasound transmit frequency). Using prototype instrumentation, it has recently been shown that microbubbles can be imaged in this manner with IVUS[51]. With these new approaches, two applications are possible: vasa vasorum imaging and molecular imaging.

Vasa vasorum imaging

It is well recognized that developing neovascular vasa vasorum is necessary for atherosclerotic plaque progression and that the microvascular status of lesions can be a marker for vulnerability to rupture[52,53]. At present, there are no established clinical tools capable of imaging coronary artery vasa vasorum[54]. Animal studies have been conducted to investigate the combination of microbubble contrast agents with prototype nonlinear IVUS systems to image vasa vasorum. In these experiments, the IVUS catheter was situated in a region of interest in an atherosclerotic rabbit aorta while contrast agent (Definity®, Bristol Myers Squibb) was released proximally in the form of a bolus through a delivery catheter. The agent was first detected within the main lumen, and then (after 5-10 second delay) within the adventitia surrounding the plaque (Figure 7). Quantification of the enhancement was statistically significant. In general, the spatial pattern of agent presence within the adventitia, and not the plaque itself, was consistent with the microvascular distribution revealed by histological sections taken in the vicinity of the imaging planes. These results indicate that contrast harmonic IVUS is capable of imaging features of vasa vasorum.

Molecular imaging

Targeted microbubble contrast agents used in conjunction with IVUS holds considerable potential for understanding the molecular status of atherosclerotic plaques, which may, in turn, impact plaque staging. A number of reports have indicated the feasibility of imaging microbubbles targeted to endothelial cell adhesion molecules[55] and fibrin[56]. These studies relied upon simple enhancement of echogenicity to determine the presence of microbubbles, and as such require the accumulation of considerable agent concentrations at target sites. The feasibility of bubble-specific imaging of targeted agent using a prototype nonlinear IVUS system was investigated[57]. The agent was an experimental biotinated, lipid encapsulated formulation comprised substantially of micron and submicron

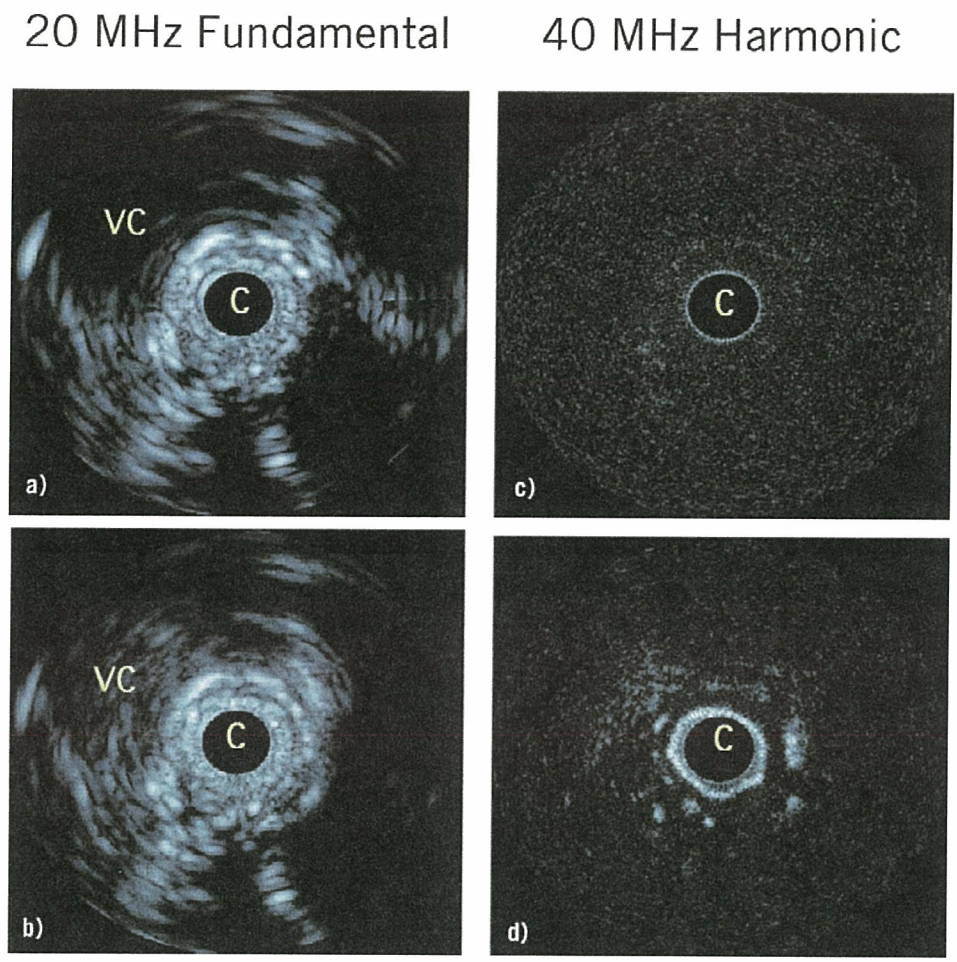

Figure 7. In vivo results in an atherosclerotic rabbit aorta using decanted Definity®. a) Fundamental mode prior to agent injection, where 'c' is the catheter, the vena cava is 'vc'. b) Fundamental mode 15 seconds post injection where changes in adventitial enhancement are not evident, except for in a region at 4 o'clock and within the vena cava. c) Harmonic mode prior to injection shows the tissue signals to be largely suppressed. d) 15 second post-injection harmonic mode shows significant adventitial enhancement, consistent with the detection of adventitial microvessels. Scale of images is 12 mm across. The dynamic range of the fundamental and harmonic images are 40 and 25 dB respectively.

sized bubbles (BG3039; Bracco Research, Geneva) targeted to an avidin coated agar substrate. Example images of tissue mimicking phantom coated with targeted contrast agents are shown in Figure 8. In fundamental (i.e. conventional 'linear' imaging) mode (Figure 8a), the agent is difficult to distinguish from background tissue signals. However, in second harmonic (not shown) and subharmonic (Figure 8b) modes the agent is clearly detected, with tissue signals suppressed below the noise floor. These results demonstrate the feasibility of harmonic imaging as a strategy for improving the sensitivity and specificity of targeted contrast agent detection at high ultrasound frequencies. Applicability of such molecular imaging approach *in vivo* still needs to be shown.

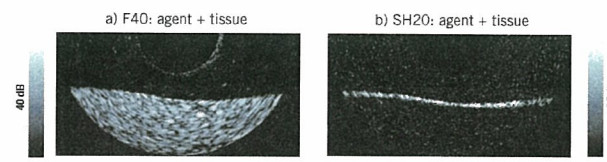

Figure 8. Agent targeted to tissue phantom in a) 40 MHz fundamental (F40) mode and b) in 20 MHz subharmonic (SH20) imaging modes. Image size 10 mm laterally, displaying half of rotational IVUS image.

Plaque characterization techniques

Structure and composition, rather than the degree of stenosis, are important characteristics of atherosclerotic plaques[58,59]. Identification of vulnerable plaques that consist of a lipid or necrotic core, covered by a thin fibrous cap, so called Thin Cap Fibro Atheromas (TCFA's) is particularly interesting, since the cap can rupture and if the necrotic core comes in touch with the blood it may create a thrombus that can occlude a vessel, causing an acute cardiovascular event. Hence, there is a need for a comprehensive imaging technique that can provide clinically relevant information both to detect and differentiate vulnerable plaques, and to determine the activity and the progression of the atherosclerotic lesion for appropriate management of the disease. Several techniques are under development for this task. Spectral analysis[60] of radiofrequency data is utilised in Virtual Histology[21], but there are several other approaches that may complement this technique, e.g. by

using self organizing maps[61]. The elastic properties of a plaque are explored by IVUS Palpography[30] and Elastography[62], but also this technique can be extended using Modulography or Thermal Strain Imaging[64]. Also combination with other imaging modalities like Photo-Acoustic Imaging[65] will likely increase sensitivity and specificity of the technique.

Intravascular photo-acoustic imaging

Catheter-based intravascular Photo-Acoustic (IVPA) imaging is being explored as a tool to identify and characterize the vulnerability of atherosclerotic plaques[66]. Integrated with intravascular ultrasound (IVUS) imaging[65], this combined technique will be capable of direct assessment of both functional and morphological properties of coronary atherosclerotic plaques, thus differentiating various types of plaques and efficiently guiding interventions with improved outcomes.

IVPA imaging is based on the detection of acoustic waves generated by laser pulses[66]. Specifically, the tissue is irradiated with short (3-10 ns) laser pulses with energy fluence (1-2 mJ/cm^2) far below the ablation threshold. As electromagnetic waves are differentially absorbed and tissue undergoes rapid thermoelastic expansion, broadband acoustic waves are generated within the irradiated volume.

Using an ultrasound detector (40-MHz IVUS catheter), these ultrasonic waves can be detected and spatially resolved to provide an image of internal tissue composition depicting the spatial distribution of optical absorbers. In IVPA imaging of arterial vessels, contrast is related to the optical absorption in intima, media, adventitia and atheromatous plaque[67]. In addition, photo-acoustic imaging has been integrated with IVUS. In this implementation, both IVPA and IVUS imaging systems utilize the same ultrasound sensor and associated receiver electronics allowing temporally consecutive, spatially concurrent ultrasonic and photo-acoustic imaging[65].

IVUS and IVPA images were obtained from an excised section of a normal rabbit artery using a 40-MHz IVUS catheter. (Figure 9) Each image covers a 6.67-mm diameter field of view with the IVUS catheter positioned at the centre. IVPA and IVUS images are spatially co-registered and show excellent correspondence. Both images illustrate the feasibility of obtaining reliable photo-acoustic signals from tissues and the ability to perform combined IVUS and IVPA imaging. The combined IVUS/IVPA image suggests that the area of functional interest can be delineated in the overall context of the vessel structure highlighting the importance and advantages of integration.

Combined IVPA and IVUS imaging can offer several advantages in imaging atherosclerotic plaques and may become an important clinical tool with sufficient sensitivity and specificity to guide coronary artery interventions. It is anticipated that IVPA/IVUS imaging may detect and differentiate different types of atherosclerotic plaques since both anatomical (morphology) and functional (activity) properties of the vessel are expected to change significantly with the presence of vulnerable plaque, and to a lesser extent with other atherosclerotic lesions. Imaging at high (few tenths of micrometers) spatial resolution should be possible in most cases since the IVPA/IVUS probe can be located inside the lumen and near the vessel wall and, therefore, high frequency ultrasound can be utilized. IVUS is routinely used in many cardiac catheterization laboratories to guide interventions, and therefore, all necessary pre-requisites for IVPA/IVUS imaging are readily available. Patients will not be subjected to any additional procedures, and the examination time will not increase to perform combined IVPA/IVUS imaging of the vessel. Both IVUS and IVPA are non-ionizing with no safety concerns. Finally, elasticity imaging or palpography[62] can also be integrated with IVUS/IVPA imaging to further enhance the clinical utility of IVUS[68,69].

IVUS RF data analysis for plaque classification using self-organizing maps

Spectral analysis of radiofrequency (RF) ultrasound signals may allow detailed assessment of plaque composition. The RF spectrum can be classified naturally using a self-organizing map (SOM) algorithm[61]. In this analysis method IVUS data are acquired with a commercially available IVUS system with a centre frequency of 40MHz. RF data are digitized and stored in a workstation using an A/D board with a sampling frequency of 500Msa/s and 8 bits resolution. After band pass filtering (15MHz-105MHz) and applying a 128 point Hamming window, the frequency spectrum is calculated for each position using an autoregressive (AR) model of order 15[70]. Optimized AR spectra are used to compute 18 spectral shape parameters for each ROI. These parameters are listed in Table 1.

The self-organizing map[71] is a neural network application used to classify these 18 parameters into seven categories which may correspond with catheter, shade, blood, fibrosis, calcium, lipid, media and others. In this study, the SOM classifier learned the spectral parameters for training. And then the SOM classifier indexed windowed areas of IVUS data based on these parameters. Finally, tis-

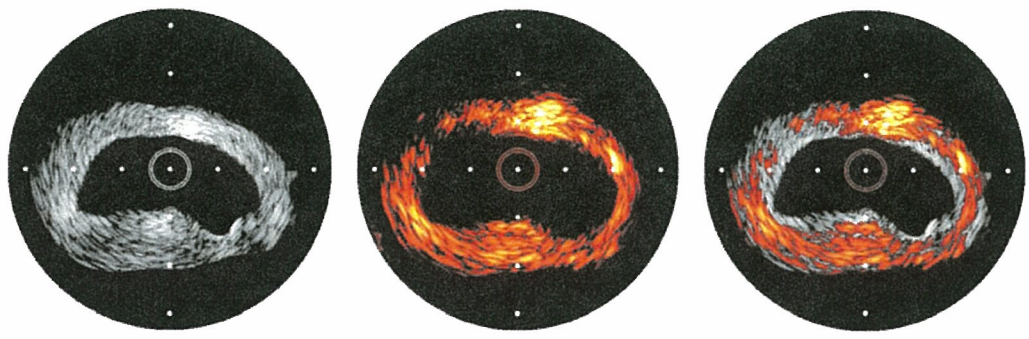

IVUS Image *IVPA Image* *Combined IVUS/IVPA image*

Figure 9. IVUS, photo-acoustic and combined image of a rabbit aorta.

Table 1. List of shape parameters classifying rf spectrum

1. Power of fundamental wave
2. Frequency of fundamental wave
3. Power of second harmonic wave
4. Frequency of second harmonic wave
5. Local minimum power between fundamental wave power and second harmonic wave power
6. Frequency of local minimum power
7. Maximum power
8. Frequency of maximum power
9. Slope from power at frequency 15MHz to fundamental wave power,
10. Corresponding y-intercept
11. Slope from fundamental wave power to local minimum power
12. Corresponding y-intercept
13. Slope from local minimum power to second harmonics power
14. Corresponding y-intercept
15. Slope from second harmonics power to 100MHz power
16. Corresponding y-intercept
17. Mean of integrated backscatter
18. ROI position at line.

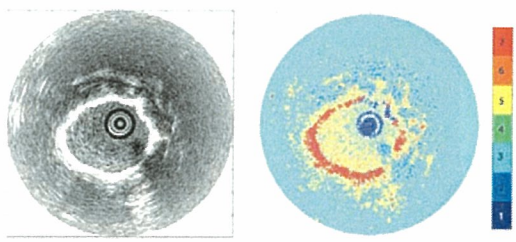

Figure 10. Conventional IVUS image (left) and color-coded image based on automatic classification by Self Organized Map (right).

sue maps were reconstructed on IVUS B-mode images based on the SOM. Table 2 gives sensitivities and specificities obtained from a limited initial data set (ref. proceedings). It is clear that extensive validation is still necessary.

Modulography: elasticity imaging of atherosclerotic coronary plaques

A new imaging technique called Modulography (concatenation of 'modulus' and 'graphy') has been developed to compute and visualize the elasticity distribution (i.e., the Young's modulus) of plaques

Table 2. Sensitivity and specificity of classified ROIs by the SOM (test data, table copied from Iwata *et al.*)

Kinds	Sensitivity	Specificity
Blood	100.0%	99.8%
Calcium	88.5%	99.8%
Catheter	99.2%	99.8%
Fibrous	88.3%	98.8%
Media	74.4%	96.7%
Others	92.8%	98.6%
Shade	88.3%	96.8%

in a so-called modulogram[63]. It directly shows the type and morphology of the main Thin Cap Fibro Atheroma (TCFA) components since the Young's modulus is a material parameter that is low for soft tissue and high for stiff tissue.

The procedure begins by computing a plaque's strain elastogram, [i.e., an image showing the deformation (strain) of the plaque caused by the pulsating blood pressure] using IVUS Elastography or Palpography[62,72,73]. Then, the plaque's modulogram is derived from the measured elastogram, as follows[74,75]: an optimization algorithm iteratively adjusts the shape and stiffness parameters of a TCFA computer-model (Figure 11), until the corresponding computer-model elastogram resembles the measured elastogram; the resulting morphology and stiffness values of the computer-model defines the modulogram. The computer-model's morphology parameters are the control-points of two deformable curves, one delineates the distal border of the lipid pool, the other the distal border of the cap; these components are assumed homogeneous and their stiffness is characterized by a YM. The inner and outer boundaries of the computer-model are contour-detected from the plaque's IVUS echogram.

Modulography successfully derived modulograms from simulated and measured elastograms of TCFA plaques. The modulograms clearly showed the morphology and stiffness of the cap and lipid pool; this information is generally not directly identifiable from the echogram or elastogram (Figure 12).

The computer-model's TCFA geometry was essential *a priori* information that allowed a stable derivation of the modulogram. However, plaques can also be heterogeneous, consisting of multiple regions of soft and stiff tissue. Therefore, we are currently generalizing Modulography, so that it works for arbitrary plaques[76]. To advance Modulography into the clinic a thorough validation study is required, as well as a pre-processing method for fully automatic assessment of proper elastograms *in vivo*[77]. As an addition to IVUS Elastography and Palpography, Modulography has strong potential

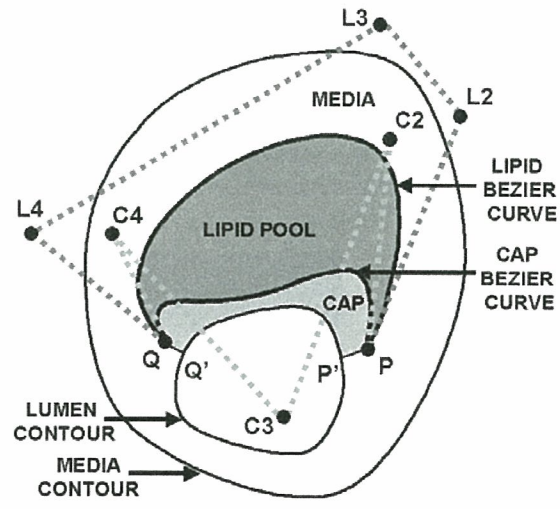

Figure 11. Computer-model of a thin-cap fibroatheroma plaque. The shape of the lipid and cap deformable Bézier curves are determined by the spatial locations of their control points. In this example there are 5 control points used for the lipid curve namely P, L2, L3, L4 and Q, and also 5 for the cap curve, namely P, C2, C3, C4 and Q.

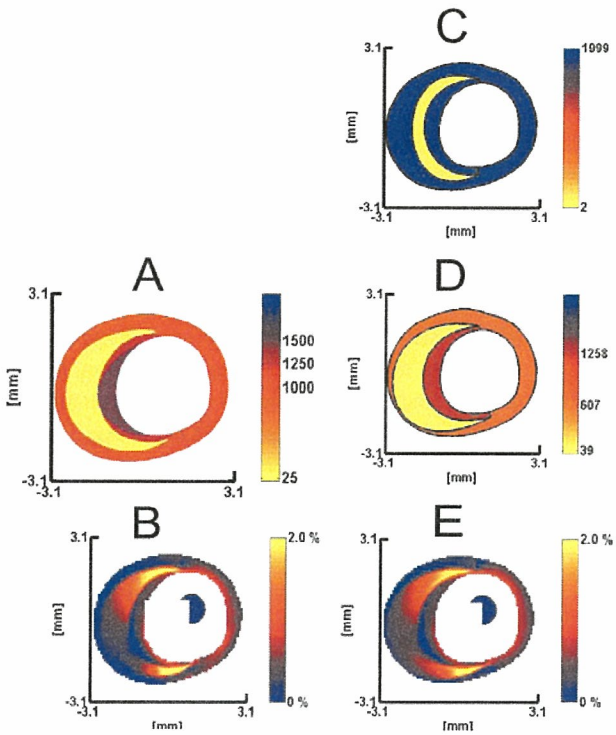

Figure 12. Modulography using a simulated strain elastogram of a thin-cap fibroatheroma plaque; its geometry and elastic material distribution was determined from tracing human coronary plaque histology. (a) Modulogram of the traced plaque; the Young's moduli of its plaque components are ELIPID=25, EMEDIA=1000 and ECAP=1250 at center / 1500 at side regions. (b) Simulated elastogram computed from a. (c) Default modulogram at the start of the optimization process. (d) Final modulogram at the end of the optimization process, derived from b. (e) Strain elastogram computed from d. Notice the resemblance between elastograms b and e, as well as the similarity between modulograms a and d. Young's moduli are in kPa and the intraluminal pressure difference is 20 mmHg. The range of each Young's modulus colour bar is (0-2000) kPa.

to become an all-in-one IVUS-based tissue characterization tool for detecting coronary plaques[73], for assessing information related to their proneness to rupture[30], and for imaging their elastic material composition, all *in vivo*.

High resolution thermal strain imaging

It is well known that lipids have a negative temperature dependence of the sound speed, whereas water-based tissues have positive temperature dependence. Controlled local temperature modulation can be used to image the spatial distribution of temporal strain produced by changes in sound speed. The opposite sign of the two different tissue types creates the contrast required for resolving the lipid-laden pool within a vulnerable plaque from surrounding water-based arterial wall. High resolution Thermal Strain Imaging (TSI) using an ultrasound (US) microscope was applied to excised porcine tissues[63,78]. Samples were placed in a temperature controlled water chamber and scanned transversely and longitudinally using a custom high resolution microscope.

An illustration of the experimental system is presented in Figure 13. Phase sensitive, correlation based speckle tracking was applied to map the spatial distribution of temporal strain across the sample. TSI

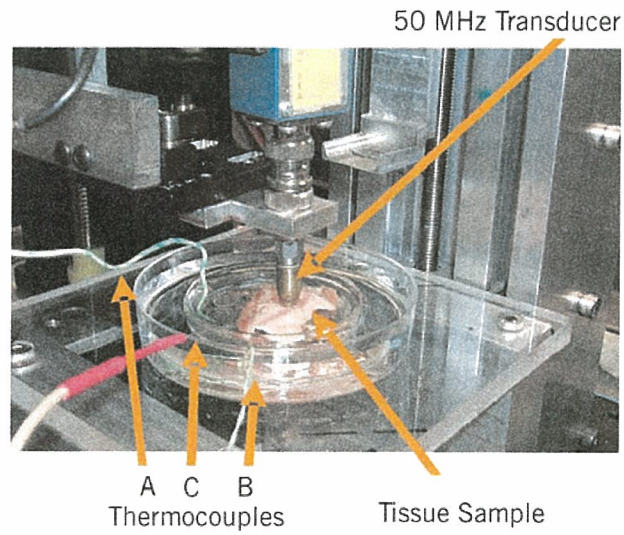

Figure 13. Experimental Set-up: Ultrasound Microscope. The coronary artery sample is held by a clip mounted at the bottom of the inner Petri dish. The outer Petri dish serves as a container for warm water to control temperature. Thermocouples monitor the temperature in the Petri dishes and inside the tissue. The single element transducer is fastened to the positioning slider driven by a stepping motor.

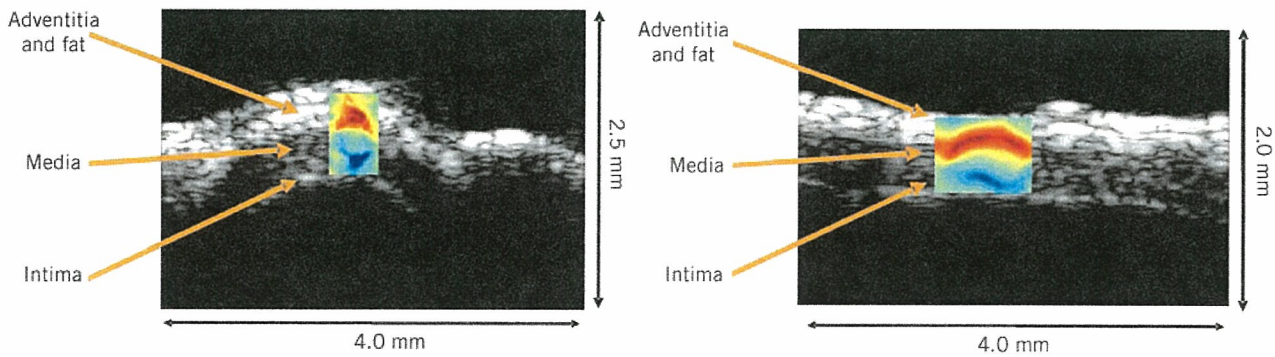

Figure 14. TSI of porcine coronary artery overlaid on the B-Scan. The top is the transverse scan and the bottom is the longitudinal scan. The dynamic range of the TSI is +/- 0.5 % over 4-5oC change in temperature. TSI images correlate well with B-Scans.

differentiated fatty tissue from the water based arterial wall and muscle with high contrast and a spatial resolution of 60 microns for a 50 MHz transducer. Both transverse and longitudinal TSI images compare well with B-Scans of arterial wall structures, including intima, media, adventitia and overlying fatty tissue, as illustrated in Figure 14. High resolution TSI images of coronary artery compare well with B-Scans of the arterial wall structure, including intima, media, adventitia and fatty tissue. This *ex-vivo* result demonstrates the feasibility of TSI for atherosclerotic plaque detection and monitoring at high resolution. A major obstacle for *in-vivo* application is tissue motion, including respiratory and cardiac motion. Motion compensation using spatial interpolation and linear least squares fitting can minimize the adverse effect of tissue motion[79].

Conclusion

In this paper several new intravascular ultrasound technologies are discussed that have been presented at the 2005 IEEE Ultrasonics symposium. All have high potential, but none is clinically available at present. Still it is clear that the development of IVUS technology is focus of attention in many research laboratories, which will result in the evolution of many high impact applications. Possibilities that are presently beyond the horizon will come within reach in the foreseeable future.

References

1. Y. Saijo, A.F.W. van der Steen, Vascular Ultrasound. Tokyo: Springer, 2003.

2. C.T. Lancee, N. Bom. Apparatus for ultrasonically examining a hollow organ, UK patent 1402192, US patent 3,827,115. 1972.

3. N. Bom, C.T. Lancee, F.C. van Egmond. An ultrasonic intracardiac scanner. *Ultrasonics,* vol. 10, pp. 72-76, 1972.

4. W.J. Gussenhoven, C.E. Essed, P. Frietman, F. Mastik, C.T. Lancee, C.J. Slager, P.W. Serruys, P. Gerritsen, H. Pieterman, N. Bom. Intravascular echographic assessment of vessel wall characteristics: A correlation with histology. *Intravascular ultrasound,* N. Bom and J. Roelandt, Eds. Dordrecht: Kluwer, 1989, pp. 105-115.

5. P.G. Yock, D.T. Linker, N.W. White, M.H. Rowe, M.R. Selmon, G.C. Robertson, T. Hinohara, J.B. Simpson. Clinical applications of intravascular ultrasound imaging in atheroma. In Intravascular ultrasound, N. Bom and J. Roelandt, Eds. Dordrecht: Kluwer, 1989, pp. 117-124.

6. C. von Birgelen, W. Li, N. Bom, P.W. Serruys. Quantitative three-dimensional intravascular ultrasound. Semin Interv Cardiol, vol. 2, pp. 25-32, 1997.

7. C. von Birgelen, M. Hartmann, G.S. Mintz, D. Baumgart, A. Schmermund, R. Erbel. Relation between progression and regression of atherosclerotic left main coronary artery disease and serum cholesterol levels as assessed with serial long-term (> or =12 months) follow-up intravascular ultrasound. *Circulation,* vol. 108, pp. 2757-62, 2003.

8. S.E. Nissen, E.M. Tuzcu, P. Schoenhagen, B.G. Brown, P. Ganz, R.A. Vogel, T. Crowe, G. Howard, C.J. Cooper, B. Brodie, C.L. Grines, A.N. DeMaria. Effect of intensive compared with moderate lipid-lowering therapy on progression of coronary atherosclerosis: a randomized controlled trial. *JAMA,* vol. 291, pp. 1071-80, 2004.

9. P.W. Serruys, M. Degertekin, K. Tanabe, A. Abizaid, J.E. Sousa, A. Colombo, G. Guagliumi, W. Wijns, W.K. Lindeboom, J. Ligthart, P.J. de Feyter, M.C. Morice. Intravascular ultrasound findings in the multicenter, randomized, double-blind RAVEL (RAndomized study with the sirolimus-eluting VElocity balloon-expandable stent in the treatment of patients with de novo native coronary artery Lesions) trial. *Circulation,* vol. 106, pp. 798-803, 2002.

10. S.G. Carlier, J.P. Marijnissen, V.L. Coen, W.J. van der Giessen, M. Sabate, J. Ligthart, A. den Boer, I.E. Cespedes, W. Li, A.F. van der Steen, P.C. Levendag, P.W. Serruys. Guidance of intracoronary radiation therapy based on dose-volume histograms derived from quantitative intravascular ultrasound. *IEEE Trans Med Imaging,* vol. 17, pp. 772-8, 1998.

11. C.J. Slager, J.J. Wentzel, F.J. Gijsen, J.C. Schuurbiers, A.C. van der Wal, A.F. van der Steen, P.W. Serruys. The role of shear stress in the generation of rupture-prone vulnerable plaques. *Nat Clin Pract Cardiovasc Med,* vol. 2, pp. 401-7, 2005.

12. R. Krams, J.J. Wentzel, J.A. Oomen, R. Vinke, J.C. Schuurbiers, P.J. de Feyter, P.W. Serruys, C.J. Slager. Evaluation of endothelial shear stress and 3D geometry as factors determining the development of atherosclerosis and remodeling in human coronary arteries in vivo. Combining 3D reconstruction from angiography and IVUS (ANGUS) with computational fluid dynamics. *Arterioscler Thromb Vasc Biol,* vol. 17, pp. 2061-5, 1997.

13. C.L. Feldman, A.U. Coskun, Y. Yeghiazarians, S. Kinlay, A. Wahle, M.E. Olszewski, J.D. Rossen, M. Sonka, J.J. Popma, J. Orav, R.E. Kuntz, P.H. Stone. Remodeling characteristics of minimally diseased coronary arteries are consistent along the length of the artery. *Am J Cardiol,* vol. 97, pp. 13-6, 2006.

14. M. O'Donnell, M.J. Eberle, D.N. Stephens, J.L. Litzza, B.M. Shapo, J.R. Crowe, C.D. Choi, J.J. Chen, D.M. W. Muller, J.A. Kovach, R.L. Lederman, R.C. Ziegenbein, C.C. Wu, K. San Vincente, D. Bleam. Catheter arrays: can intravascular ultrasound make a difference in managing coronary artery disease. *IEEE Ultrasonics Symposium,* 1447-1456 1997.

15. A.F.W. van der Steen, E.I. Cespédes, C.L. de Korte, S.G. Carlier, W. Li, F. Mastik, C.T. Lancée, J. Borsboom, F. Lupotti, R. Krams, P.W. Serruys, N. Bom. Novel developments in intravascular imaging. *IEEE Ultrasonics Symposium,* 1733-1742 1998.

16. M. O'Donnell. Phased array beam forming from a circular array: applications to imaging of coronary arteries. *IEEE Ultrasonicsl Symposium,* pp. 637-640, 1991.

17. U. Demirci, A.S. Ergun, O. Oralkan, M. Karaman, B.T. Khuri-Yakub. Forward-viewing CMUT arrays for medical Imaging. *IEEE Transactions on Ultrasonics Ferroelectrics and Frequency Control,* vol. 51, pp. 887-895, 2004.

18. Y. Wang, D.N. Stephens, M. O'Donnell. Optimizing the beam pattern of a forward-viewing ring-annular ultrasound array for intravascular imaging. *IEEE Transactions on Ultrasonics Ferroelectrics and Frequency Control,* vol. 49, pp. 1652-1664, 2002.

19. J.R. Crowe, B.M. Shapo, D.N. Stephens, D. Bleam, M.J. Eberle, C.C. Wu, D.M.W. Muller, J.A. Kovatch, R.L. Lederman, M. O'Donnell. Coronary artery flow imaging with an Intraluminal array. *IEEE Ultrasonics Symposium,* pp. 1481-1484, 1996.

20. E.I. Cespédes, W. Li, F. Mastik, A.F.W. van der Steen, S.G. Carlier, R.H. van Bremen, M. Eberle, N. Bom. Intravascular Power Flow Imaging: Theory and potentials for planimetry. *IEEE Ultrasonics Symposium,* pp. 1273-1276, 1997.

21. W. Li, A.F. van der Steen, C.T. Lancee, I. Cespedes, N. Bom. Blood flow imaging and volume flow quantitation with intravascular ultrasound. *Ultrasound Med Biol,* vol. 24, pp. 203-14, 1998.

22. J.R. Crowe, M. O'Donnell. .Quantitative blood speed imaging with intravascular ultrasound. *IEEE Trans Ultrason Ferroelectr Freq Control,* vol. 48, pp. 477-87, 2001.

23. S.G. Carlier, W. Li, I. Cespedes, A.F. van der Steen, J.N. Hamburger, N. Bom, P. W. Serruys. Images in cardiovascular medicine. Simultaneous morphological and functional assessment of a renal artery stent intervention with intravascular ultrasound. *Circulation,* vol. 97, pp. 2575-6, 1998.

24. S.L. Bridal, P. Fornes, P. Bruneval, G. Berger. Parametric (integrated backscatter and attenuation) images constructed using backscattered radio frequency signals (25-56 MHz) from human aortae in vitro. *Ultrasound Med Biol,* vol. 23, pp. 215-29, 1997.

25. T. Spencer, M.P. Ramo, D.M. Salter, T. Anderson, P.P. Kearney, G.R. Sutherland, K.A. Fox, W.N. McDicken. Characterisation of atherosclerotic plaque by spectral analysis of intravascular ultrasound: an in vitro methodology. *Ultrasound Med Biol,* vol. 23, pp. 191-203, 1997.

26. A. Nair, B. D. Kuban, E. M. Tuzcu, P. Schoenhagen, S.E. Nissen, D.G. Vince, Coronary plaque classification with intravascular ultrasound radiofrequency data analysis. *Circulation,* vol. 106, pp. 2200-2206, 2002.

27. S.A. Wickline, J.G. Miller, D. Recchia, A.M. Sharkey, S.L. Bridal, D.H. Christ. Beyond intravascular imaging: Quantitative ultrasonic tissue characterization of vascular pathology. *IEEE Ultrasonics Symposium,* pp. 1589-1598, 1994.

28. L.K. Ryan, F.S. Foster. Ultrasonic measurement of differential displacement and strain in a vascular model. *Ultrason Imaging,* vol. 19, pp. 19-38, 1997.

29. C.L. de Korte, E.I. Cespedes, A.F. van der Steen, G. Pasterkamp, N. Bom. Intravascular ultrasound elastography: assessment and imaging of elastic properties of diseased arteries and vulnerable plaque. *Eur J Ultrasound,* vol. 7, pp. 219-24, 1998.

30. J.A. Schaar, C.L. De Korte, F. Mastik, C. Strijder, G. Pasterkamp, E. Boersma, P.W. Serruys, A.F.W. Van Der Steen. Characterizing vulnerable plaque features with intravascular elastography. *Circulation,* vol. 108, pp. 2636-41, 2003.

31. Y. Saijo, S. Tanaka, N. Owada, Y. Akino, S. Nitta. Tissue velocity imaging of coronary artery by rotating-type intravascular ultrasound. *Ultrasonics,* vol. 42, pp. 753-757, 2004.

32. B.M. Shapo, J.R. Crowe, R. Erkamp, S.Y. Emelianov, M.J. Eberle, M. O'Donnell. Strain imaging of coronary arteries with intraluminal ultrasound: experiments on an inhomogeneous phantom. *Ultrason Imaging,* vol. 18, pp. 173-91, 1996.

33. O. Oralkan, A.S. Ergun, J.A. Johnson, M. Karaman, U. Demirci, K. Kaviani, T.H. Lee, B.T. Khuri-Yakub. Capacitive micromachined ultrasonic transducers: Next-generation arrays for acoustic imaging? *IEEE Transactions on Ultrasonics Ferroelectrics and Frequency Control,* vol. 49, pp. 1596-1610, 2002.

34. F.L. Degertekin, R.O. Guldiken, M. Karaman. Micromachined Capacitive Transducer Arrays for Intravascular Ultrasound Imaging, presented at SPIE Symposium on MOEMS Display and Imaging Systems, 2005.

35. D.T. Yeh, O. Oralkan, I.O. Wygant, M. O'Donnell, B.T. Khuri-Yakub. 3-D Ultrasound Imaging Using Forward Viewing CMUT Ring Arrays for Intravascular and Intracardiac Applications. *IEEE Ultrasonics Symposium,* pp. 783-786, 2005.

36. F.L. Degertekin, M. Karaman, R.O. Guldiken. Forward-Looking IVUS Imaging Using an Annular-Ring CMUT Array. *IEEE Ultrasonics Symposium,* pp. 129-132, 2005.

37. J. Knight, J. McLean, F.L. Degertekin. Low temperature fabrication of immersion capacitive micromachined ultrasonic transducers on silicon and dielectric substrates. *IEEE Transactions on Ultrasonics Ferroelectrics and Frequency Control,* vol. 51, pp. 1324-1333, 2004.

38. F.L. Degertekin, R.O. Guldiken, M. Karaman. Annular-ring CMUT arrays for forward-looking IVUS: transducer characterization and imaging. *IEEE Trans Ultrason Ferroelectr Freq Control,* vol. 53, pp. 474-482, 2006.

39. H. ten Hoff, A. Korbijn, T.H. Smith, J.F. Klinkhamer, N. Bom. Imaging artifacts in mechanically driven ultrasound catheters. *Int J Card Imaging,* vol. 4, pp. 195-9, 1989.

40. C.T. Lancee, N. Bom, J. Roelandt. Future directions in intravascular ultrasound: from micro-motors to imaging guidewire systems. *Echocardiography,* vol. 12, pp. 275-81, 1995.

41. N. Bom, S.G. Carlier, A.F. van der Steen, C.T. Lancee. Intravascular scanners. *Ultrasound Med Biol,* vol. 26 Suppl 1, pp. S6-9, 2000.

42. T. Moriya, Y. Akano, Y. Furukawa, A. Nakajima. Development of a Miniature Ultrasonic Motor Using a Helical Coil as a Stator. *IEEE Ultrasonics Symposium,* pp. 1546-1549, 2005.

43. M.A. Averkiou, D.N. Roundhill, J.E. Powers. A new imaging technique based on the nonlinear properties of tissues. *IEEE Ultrasonics Symposium,* pp. 1561-1566, 1997.

44. B. Ward, A.C. Baker, V.F. Humphrey. Nonlinear propagation applied to the improvement of lateral resolution in medical ultrasound scanners, presented at World Congress on Ultrasonics, 1995.

45. E.W. Cherin, J.K. Poulsen, A.F. W. van der Steen, P. Lum, F.S. Foster. Experimental characterization of fundamental and second harmonic beams for a high-frequency ultrasound transducer. *Ultrasound Med Biol,* vol. 28, pp. 635-46, 2002.

46. A.F.W. van der Steen, J.K. Poulsen, E. Cherin, F.S. Foster. Harmonic imaging at high frequencies for IVUS. *IEEE Ultrasonics Symposium,* pp. 1537-1540, 1999.

47. M.E. Frijlink, D.E. Goertz, A.F.W. van der Steen. Reduction of stent artifacts using high-frequency harmonic ultrasound imaging. *Ultrasound Med Biol,* vol. 31, pp. 1335-1342, 2005.

48. M.E. Frijlink, D.E. Goertz, H.J. Vos, E. Droog, G. Blacquière, A. Gisolf, A.F.W. van der Steen. Harmonic Intravascular Ultrasound Imaging with a dual-frequency catheter. *IEEE Ultrasonics Symposium,* pp. 241-244, 2005.

49. H.J. Vos, M.E. Frijlink, E. Droog, D.E. Goertz, G. Blacquière, A. Gisolf, N. de Jong, A.F.W. van der Steen. Transducer for Harmonic Intravascular Ultrasound Imaging. *IEEE Trans Ultrason Ferroelectr Freq Control,* vol. 52, pp. 2418-2422, 2005.

50. B.B. Goldberg, Ultrasound contrast agents: Basic principles and clinical applications in echocardiography, vol. Second edition. London: Martin Dunitz, 2001.

51. D.E. Goertz, M.E. Frijlink, N. de Jong, A.F.W. van der Steen. Nonlinear intravascular ultrasound contrast imaging. *Ultrasound Med Biol,* in press.

52. K.S. Moulton. Plaque angiogenesis: its functions and regulation. *Cold Spring Harb Symp Quant Biol,* vol. 67, pp. 471-82, 2002.

53. P.R. Moreno, K.R. Purushothaman, V. Fuster, D. Echeverri, H. Truszczynska, S.K. Sharma, J.J. Badimon, W.N. O'Connor. Plaque neovascularization is increased in ruptured atherosclerotic lesions of human aorta: implications for plaque vulnerability. *Circulation,* vol. 110, pp. 2032-8, 2004.

54. D.E. Goertz, M.E. Frijlink, D. Tempel, R. Krams, P. W. Serruys, F. ten Cate, J.A. Schaar, N. de Jong, A.F.W. van der Steen. Contrast harmonic intravascular ultrasound: a feasibility study for vasa vasorum imaging. *Investigative Radiology,* submitted.

55. F.S. Villanueva, R.J. Jankowski, S. Klibanov, M.L. Pina, S.M. Alber, S.C. Watkins, G.H. Brandenburger, W.R. Wagner. Microbubbles targeted to intercellular adhesion molecule-1 bind to activated coronary artery endothelial cells. *Circulation,* vol. 98, pp. 1-5, 1998.

56. S.M. Demos, H. Alkan-Onyuksel, B.J. Kane, K. Ramani, A. Nagaraj, R. Greene, M. Klegerman, D.D. McPherson. In vivo targeting of acoustically reflective liposomes for intravascular and transvascular ultrasonic enhancement. *J Am Coll Cardiol,* vol. 33, pp. 867-75, 1999.

57. D.E. Goertz, J.E.T. van Wamel, M.E. Frijlink, N. de Jong, A.F.W. van der Steen. Nonlinear Imaging of Targeted Microbubbles with Intravascular Ultrasound. *IEEE Ultrasonics Symposium,* pp. 2003-2006, 2005.

58. J.A. Schaar, J.E. Muller, E. Falk, R. Virmani, V. Fuster, P.W. Serruys, A. Colombo, C. Stefanadis, S. Ward Casscells, P.R. Moreno, A. Maseri, A.F. van der Steen. Terminology for high-risk and vulnerable coronary artery plaques. Report of a meeting on the vulnerable plaque, June 17 and 18, 2003, Santorini, Greece. *Eur Heart J,* vol. 25, pp. 1077-82, 2004.

59. M. Naghavi, P. Libby, E. Falk, S.W. Casscells, S. Litovsky, J. Rumberger, J.J. Badimon, C. Stefanadis, P. Moreno, G. Pasterkamp, Z. Fayad, P.H. Stone, S. Waxman, P. Raggi, M. Madjid, A. Zarrabi, A. Burke, C. Yuan, P.J. Fitzgerald, D.S. Siscovick, C.L. de Korte, M. Aikawa, K.E. Juhani Airaksinen, G. Assmann, C.R. Becker, J.H. Chesebro, A. Farb, Z.S. Galis, C. Jackson, I.K. Jang, W. Koenig, R.A. Lodder, K. March, J. Demirovic, M. Navab, S.G. Priori, M.D. Rekhter, R. Bahr, S.M. Grundy, R. Mehran, A. Colombo, E. Boerwinkle, C. Ballantyne, W. Insull, Jr., R.S. Schwartz, R. Vogel, P.W. Serruys, G.K. Hansson, D.P. Faxon, S. Kaul, H. Drexler, P. Greenland, J.E. Muller, R. Virmani, P.M. Ridker, D.P. Zipes, P.K. Shah, J.T. Willerson. From vulnerable plaque to vulnerable patient: a call for new definitions and risk assessment strategies: Part I. *Circulation,* vol. 108, pp. 1664-72, 2003.

60. Z.A. Fayad, V. Fuster. Clinical imaging of the high-risk or vulnerable atherosclerotic plaque. *Circ Res,* vol. 89, pp. 305-16, 2001.

61. T. Iwamoto, A. Tanaka, Y. Saijo, M. Yoshizawa. Coronary Plaque Classification through Intravascular Ultrasound Radiofrequency Data Analysis Using Self-organizing Map. *IEEE Ultrasonics Symposium,* pp. 2054-2057, 2005.

62. C.L. de Korte, M.J. Sierevogel, F. Mastik, C. Strijder, J.A. Schaar, E. Velema, G. Pasterkamp, P.W. Serruys, A.F.W. van der Steen. Identification of atherosclerotic plaque components with intravascular ultrasound elastography in vivo: a Yucatan pig study. *Circulation,* vol. 105, pp. 1627-1630, 2002.

63. R.A. Baldewsing, F. Mastik, J.A. Schaar, A.F.W. van der Steen. Young's Modulus Reconstruction and Delineation of Vulnerable Atherosclerotic Plaque Components. *IEEE Ultrasonics Symposium,* pp. 249-252, 2005.

64. K. Kim, R. Witte, M. O'Donnell. Arterial Lipid Characterization by High Resolution TSI. *IEEE Ultrasonics Symposium,* pp. 137-140, 2005.

65. S. Sethuraman, S.R. Aglyamov, J.H. Amirian, R.W. Smalling, S.Y. Emelianov. Development of a combined intravascular ultrasound and photoacoustic imaging system, presented at Proceedings of the 2006 SPIE Photonics West Symposium: Photons Plus Ultrasound: Imaging and Sensing, 2006.

66. S. Sethuraman, S.R. Aglyamov, J.H. Amirian, R.W. Smalling, S.Y. Emelianov. Intravascular photoacoustic imaging to detect and differentiate atherosclerotic plaques. *IEEE Ultrasonics Symposium,* pp. 133-136, 2005.

67. P.C. Beard, T.N. Mills. Characterization of post mortem arterial tissue using time-resolved photoacoustic spectroscopy at 436, 461 and 532 nm. *Phys Med Biol,* vol. 42, pp. 177-98, 1997.

68. S. Sethuraman, S.R. Aglyamov, J.H. Amirian, R.W. Smalling, S.Y. Emelianov. An integrated ultrasound-based intravascular imaging of atherosclerosis, presented at Proceedings of the Fourth International Conference on the Ultrasonic Measurement and Imaging of Tissue Elasticity, 2005.

69. S.Y. Emelianov, S.R. Aglyamov, J. Shah, S. Sethuraman, W.G. Scott, R. Schmitt, M. Motamedi, A. Karpiouk, A. Oraevsky. Combined ultrasound, optoacoustic and elasticity imaging, presented at Proceedings of the 2004 SPIE Photonics West Symposium: Photons Plus Ultrasound: Imaging and Sensing, 2004.

70. T. Baldeweck, P. Laugier, A. Herment, G. Berger. Application of Autoregressive Spectral-Analysis for Ultrasound Attenuation Estimation - Interest in Highly Attenuating Medium. *IEEE Transactions on Ultrasonics Ferroelectrics and Frequency Control,* vol. 42, pp. 99-110, 1995.

71. T. Kohonen, *Self-Organizing Maps,* vol. 30, 3rd ed. Berlin, Heidelberg, New York: Springer, 2001.

72. M. Doyley, F. Mastik, C.L. de Korte, S. Carlier, E. Cespedes, P. Serruys, N. Bom, A.F.W. van der Steen. Advancing intravascular ultrasonic palpation towards clinical applications. *Ultrasound Med Biol,* vol. 27, pp. 1471-1480, 2001.

73. J.A. Schaar, E. Regar, F. Mastik, E.P. McFadden, F. Saia, C. Disco, C.L. de Korte, P.J. de Feyter, A.F.W. van der Steen, P.W. Serruys. Incidence of vulnerable plaque patterns in humans: assessment with three-dimensional intravascular palpography and correlation with clinical presentation. *Circulation,* vol. 109, pp. 2716-2719, 2004.

74. R.A. Baldewsing, F. Mastik, J.A. Schaar, P.W. Serruys, A.F.W. van der Steen. Young's modulus reconstruction of vulnerable atherosclerotic plaque components using deformable curves. *Ultrasound in Med Biol,* vol. 32, pp. 201-210, 2005.

75. R.A. Baldewsing, J.A. Schaar, F. Mastik, C.W.J. Oomens, A.F.W. van der Steen. Assessment of vulnerable plaque composition by matching the deformation of a parametric plaque model to measured plaque deformation. *IEEE Trans Med Imaging,* vol. 24, pp. 514-528, 2005.

76. R.A. Baldewsing, F. Mastik, J.A. Schaar, A.F.W. van der Steen. A compounding method for reconstructing the heterogeneous Young's modulus distribution of atherosclerotic plaques from their radial strain. Proceedings of the Fourth International Conference on the Ultrasonic Measurement and Imaging of Tissue Elasticity, pp. 68, 2005.

77. K.Y.E. Leung, R.A. Baldewsing, F. Mastik, J.A. Schaar, A. Gisolf, A.F.W. van der Steen. Motion Compensation for Intravascular Ultrasound Palpography. *IEEE Trans Ultrason Ferroelectr Freq Control,* vol. 53 in press, 2005.

78. Y. Shi, R.S. Witte, M. O'Donnell. Identification of vulnerable atherosclerotic plaque using IVUS-based thermal strain imaging. *IEEE Transactions on Ultrasonics Ferroelectrics and Frequency Control,* vol. 52, pp. 844-850, 2005.

79. Y. Shi, F.J. de Ana, S.J. Chetcuti, M. O'Donnell. Motion artifact reduction for IVUS-based thermal strain imaging. *IEEE Transactions on Ultrasonics Ferroelectrics and Frequency Control,* vol. 52, pp. 1312-1319, 2005.

Available online at www.sciencedirect.com
SCIENCE DIRECT®
Ultrasonics 44 (2006) 297–301
Ultrasonics
www.elsevier.com/locate/ultras

Does decalcification alter the tissue sound speed of rabbit supraspinatus tendon insertion? In vitro measurement using scanning acoustic microscopy

Hirotaka Sano [a,*], Koshi Hattori [a], Yoshifumi Saijo [b], Shoichi Kokubun [a]

[a] *Department of Orthopaedic Surgery, Tohoku University School of Medicine, 1-1 Seiryomachi, Aoba-ku, Sendai 980-8574, Japan*
[b] *Department of Medical Engineering and Cardiology, Institute of Development, Aging and Cancer, Tohoku University, Japan*

Received 28 October 2005; received in revised form 13 March 2006; accepted 21 March 2006
Available online 18 April 2006

Abstract

Failure of the tendon or ligament insertions is one of the most common injuries in the Orthopaedic field. To elucidate the pathogenesis of those injuries, the authors had attempted to measure the tissue sound speed that could be correlated to its elasticity using scanning acoustic microscopy (SAM). For the application of SAM to tendon or ligament insertions, it was necessary to determine the role of decalcification in SAM measurements since mineralized tissues including bone or mineralized fibrocartilage were present at the insertion site.

To assess whether decalcification alters the tissue sound speed or not, supraspinatus tendon insertion of six Japanese white rabbits were measured with SAM operating in the frequency range of 50–150 MHz. Right supraspinatus tendons attached to the humeral head were cut into two pieces at the center of the tendon. Then, they were fixed with 10% neutralized formalin for 12 h. In each specimen, medial half was not decalcified, while lateral half was decalcified with ethylene-diamine-tetra-acetic acid (EDTA). After embedding in paraffin, 5 μm thick specimens were prepared for the measurement using SAM. The mean sound speed in each histologic zone was evaluated, and subsequently compared to that measured in the undecalcified and the decalcified specimens.

Mean sound speed of non-mineralized fibrocartilage was 1544 m/s in the undecalcified specimens, while the value of 1541 m/s was determined in the decalcified ones. On the other hand, it decreased 2–3% after decalcification in the mineralized tissue including mineralized fibrocartilage and bone (mineralized fibrocartilage: undecalcified = 1648 m/s, decalcified = 1604 m/s; bone: undecalcified = 1716 m/s, decalcified = 1677 m/s). However, no significant differences were found between the undecalcified and the decalcified specimens (non-mineralized fibrocartilage: $p = 0.84$, mineralized fibrocartilage: $p = 0.35$, bone: $p = 0.28$). These results indicate that SAM could be applied to determine the properties of the tendon or the ligament insertions after decalcification with EDTA.

Although SAM is applicable only for in vitro experimental study, it is expected that these data will contribute to better understanding concerning the biomechanics of tendon or ligament insertions as well as the pathogenesis of their failure at a microscopic level.

Keywords: Scanning acoustic microscopy; Sound speed; Supraspinatus tendon; Insertion; Decalcification

1. Introduction

1.1. Background of the study

Scanning acoustic microscopy (SAM) has been used to assess the high-frequency acoustic properties of various types of soft tissue, representing complex histologic structures, i.e. cardiac muscles, arterial plaques and vascular

* Corresponding author. Tel.: +81 22 717 7242; fax: +81 22 717 7248.
E-mail address: staka@mail.tains.tohoku.ac.jp (H. Sano).

0041-624X/$ - see front matter © 2006 Elsevier B.V. All rights reserved.
doi:10.1016/j.ultras.2006.03.002

walls, etc. [1–3]. One of the major advantages of SAM is that tissue sound speed can be measured with formalin-fixed and paraffin-embedded glass slides. This makes it possible to compare the two-dimensional distribution of the tissue sound speed to the histologic structure of a given specimen.

Failure of the tendon or ligament insertions is one of the most common injuries in the orthopaedic field; i.e. rotator cuff tear, ruptures of anterior cruciate ligament or anterior talofibular ligament, etc. To elucidate the pathogenesis and to optimize the surgical treatment for those injuries, both the histologic structure and the biomechanical characteristics of the insertion should be determined. Histologically, it has been well known that a transition zone from soft tissue to bone occurs at the injury site [4]. Specifically, this transition consists of four zones including tendon proper, non-mineralized fibrocartilage, mineralized fibrocartilage and bone. Unfortunately, however, little is known about the biomechanical characteristics of the insertion site because of such inhomogeneous histologic structure.

Based on these facts, the authors first applied SAM to the supraspinatus tendon insertion, where most of rotator cuff tears were seen [5,6]. Despite technical difficulties associated with the tissue preparation, we have successfully measured tissue sound speed at the tendon insertion site. In the specimens that contained mineralized tissue including bone or mineralized fibrocartilage, decalcification was usually applied so as not to cause artifacts during the cutting process. Since, however, the effects of decalcification on the results of SAM measurement had not been investigated yet, we did not decalcify the specimens but just removed bony tissue as much as possible at the time of dissection [5,6].

The results of these pilot investigations indicated that the role of decalcification in SAM measurement must be carefully examined. Especially, we hoped to learn whether decalcification alters the tissue sound speed at the supraspinatus tendon insertion or not.

2. Materials and methods

2.1. Preparation of the specimens

Supraspinatus tendon insertions of six Japanese white rabbits were used for the current study. All these animals were 12 month-old males and their average body weight was 2.3 kg (range: 2.2–2.4 kg). After euthanasia with overdosed pentobarbital, right supraspinatus tendons attached to the humeral head were collected. The specimens were cut into two pieces at the center of supraspinatus tendon in line with its fibers and bony tissue was carefully removed except for the insertion site. Then, they were fixed with 10% neutralized formalin for 12 h.

In each animal, medial half of the specimen was not decalcified, while lateral half of the specimen was decalcified with ethylene-diamine-tetra-acetic acid (EDTA). After embedding in paraffin, the specimen were cut at a thickness of 5 μm both for the histologic staining and for the measurement with SAM.

2.2. Histologic staining

Haematoxylin-eosin (HE) staining was routinely employed to assess the overall histologic structure. Both the zone of non-mineralized fibrocartilage and that of the mineralized fibrocartilage were determined histologically. Photographs were taken under the microscope, which were trimmed thereafter to create histologic images with zones identical to those of the SAM measurements.

2.3. SAM measurement

A specially developed SAM system in Tohoku University, operating in the frequency range of 50–150 MHz, was used for this study (Fig. 1). The sections for SAM measurements were mounted on glass slides but not covered by cover slips. The paraffin was removed from the sections by the graded alcohol method prior to the ultrasonic measurement. Distilled water was used as the coupling medium, which maintained the specimen at 20 °C during the measurement procedure. A single ultrasound pulse width 5 ns was emitted and received by the same transducer above the specimen. The reflections from the tissue surface and those from the interface between the tissue and glass were introduced into a digital oscilloscope. Four values of the time taken for a pulse response at the same point were averaged in the oscilloscope in order to reduce the noise in the measurement. The transducer was mounted on an X–Y stage with a microcomputer board that was driven by the computer installed in the digital oscilloscope. The X-scan was driven by a linear servo motor, and the Y-scan was driven by a stepping motor. Finally, two-dimensional distribution of sound speed in a specimen measuring 2.4×2.4 mm were visualized using 300×300 pixels. The

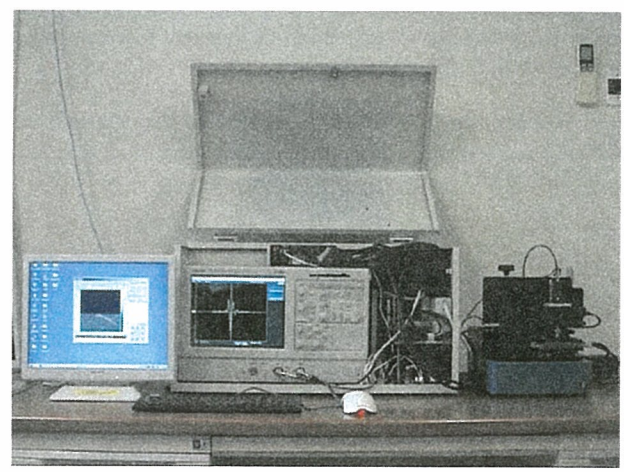

Fig. 1. System of scanning acoustic microscopy (SAM). The two-dimensional distribution of sound speed in 2.4 mm × 2.4 mm square field can be measured with the tabletop type SAM.

overall uncertainty of the measurement using this system was approximately 15 m/s [7,8].

It is known that the sound speed measured by SAM is defined by the following equation (Eq. (1)):

$$C = (1/C_w - \theta/2\pi fd)^{-1} \quad (1)$$

where C is the sound speed in the specimen, C_w is the sound speed in the coupling medium, f is the frequency, d is the thickness of the specimen and θ is the phase shift. This equation can be modified to describe the relationship between the acoustics and a solid material:

$$C = \sqrt{\frac{E(1-\sigma)}{\rho(1+\sigma)(1-2\sigma)}} \quad (2)$$

where E is the Young's modulus, ρ the density and σ the Poisson's ratio. Eq. (2) shows that the tissue sound speed measured using the SAM is directly proportional to the square value of its Young's modulus.

Since the fibrocartilage was the most distinct in the deep part of the tendon insertion, we determined to focus on the articular half of the insertion site [9]. The data of the sound speed obtained were converted into color signals on the computer. Two-dimensional distribution pattern of the sound speed was displayed and saved as an image file using a color-coded scale, which made it convenient to compare visually the value of sound speed between the undecalcified and the decalcified specimens. Moreover, the data was also saved as an image file with gray-scale to quantify the sound speed of each zone.

2.4. Data interpretation

In each specimen, a gray-scale image was imported to the image analyzing software, Image J (version 1.34 s). Since the sound speed was converted to the gray-scale data in those images, the sound speed could be calculated using the degree of density. The zones of non-mineralized fibrocartilage, mineralized fibrocartilage and bone were determined histologically. In each zone, the average value of the density (between 0 and 255) was calculated three times using the analysis option, "histogram" and the mean value of those three data (*mean density*) was used for further analysis. Then, the *mean density* in each histologic zone was converted again to the sound speed (*mean sound speed*). The *mean sound speed* was compared between the undecalcified and the decalcified specimens to find out whether decalcification alters the sound speed in SAM measurement.

For statistical analysis, paired t-test was used for determining the statistical differences between the undecalcified and the decalcified specimens. The p-value less than 0.05 were considered as statistically significant.

3. Results

The two-dimensional distribution of sound speed indicated almost identical pattern between the undecalcified and the decalcified specimens (Figs. 2 and 3). Non-mineralized fibrocartilage represented the lowest value in sound speed among three zones of the supraspinatus tendon insertion. *Mean sound speed* in this zone was 1544 m/s in the undecalcified specimens and 1541 m/s in the decalcified specimens. No significant difference was found between the undecalcified and the decalcified specimens ($p = 0.84$).

In the mineralized tissue (mineralized fibrocartilage and bone), sound speed decreased 2–3% after decalcification. The *mean sound speed* of mineralized fibrocartilage was 1648 m/s in the undecalcified specimens and 1604 m/s in the decalcified specimens. In bone, it was 1716 m/s in the undecalcified specimens and 1677 m/s in the decalcified specimens (Fig. 4). However, no significant differences were found statistically between the undecalcified and the decalcified specimens (mineralized fibrocartilage: $p = 0.35$, bone: $p = 0.28$).

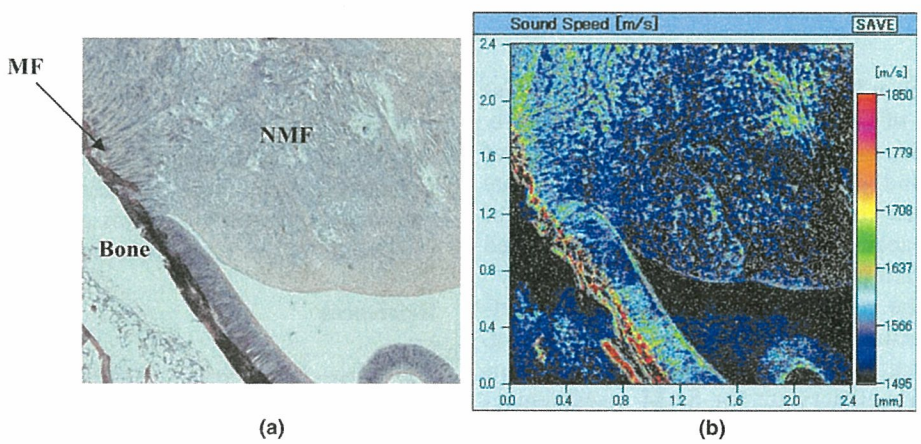

(a) (b)

Fig. 2. Sound speed in undecalcified specimen (Rabbit No. 3). (a) haematoxylin-eosin, (b) sound speed. Non-mineralized fibrocartilage is depicted with blue and black. On the other hand, mineralized fibrocartilage and bone were depicted with green and red (NMF: non-mineralized fibrocartilage, MF: mineralized fibrocartilage).

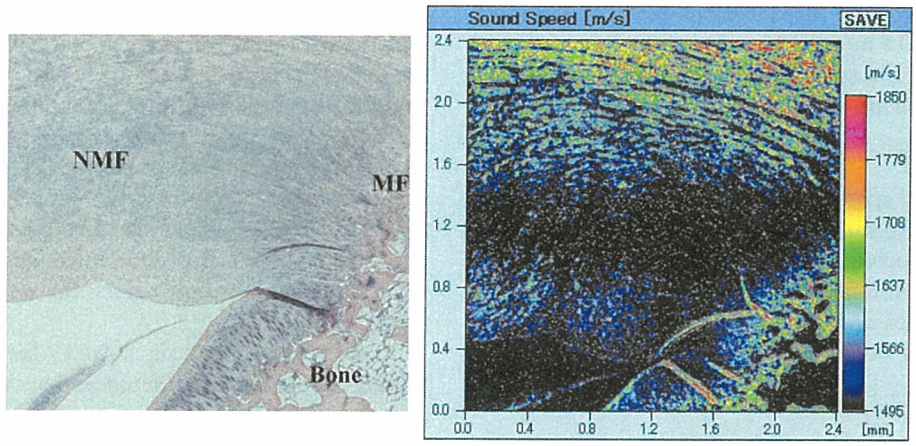

Fig. 3. Sound speed in decalcified specimen (Rabbit No. 3). (a) haematoxylin-eosin, (b) sound speed. In decalcified specimens, non-mineralized fibrocartilage is also depicted with blue and black. In mineralized tissue, both mineralized fibrocartilage and bone are depicted green and yellow.

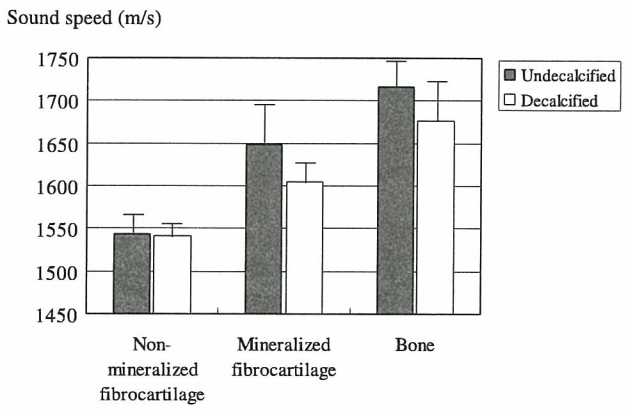

Fig. 4. *Mean sound speed* in each histologic zone. In non-mineralized fibrocartilage, the sound speed measured with the decalcified specimens is almost identical to that measured with the undecalcified specimens. On the other hand, it decreases 2–3% both in zones of mineralized fibrocartilage and bone after decalcification with ethylene-diamine-tetra-acetic acid.

4. Discussion

To use the data from SAM measurement, it is important to know the effects of tissue preparation on the measurement results. In 1996, Sasaki et al. evaluated the effect of formalin fixation and paraffin embedding using normal kidney tissue. In their results, the relative relationships of the high-frequency acoustic properties was well preserved after these preparation process [10].

Unfortunately, the role of decalcification for the outcome of SAM measurements has not been clarified yet. Other researchers mainly used the undecalcified specimens embedded in methylmethacrylate for SAM measurement [11–13]. However, there are several disadvantages when using this type of undecalcified specimens. First, preparation of sections including the process of grinding and polishing is very time consuming. Second, it is technically difficult to control the thickness of the sections constant during the preparation process. Uneven thickness of the section might cause measurement errors since tissue sound speed is affected by the thickness of the specimens (Eq. (1)). Third, it is difficult to identify the shape of each cell with the grinded undecalcified sections, which makes it difficult to perform histologic observation. Especially, in immunohistochemical staining, most antibodies have been developed for formalin-fixed and paraffin-embedded specimens and they cannot be used for grinded undecalcified specimens. All these disadvantages make it difficult to compare the tissue sound speed to the histologic or the immunohistochemical characteristics.

Our study demonstrated that the sound speed of soft tissue including non-mineralized fibrocartilage was not altered by decalcification. Although it decreased 2–3% after decalcification in the mineralized tissue including mineralized fibrocartilage and bone, no significant differences were found between the undecalcified and the decalcified specimens (Fig. 4). These results indicate that SAM could be applied to determine the properties of the tendon or the ligament insertions after decalcification with ethylene-diamine-tetra-acetic acid (EDTA).

Although SAM is applicable only for in vitro experimental study, it is expected that these data will contribute to better understanding concerning the biomechanics of tendon or ligament insertions as well as the pathogenesis of their failure at a microscopic level.

References

[1] Y. Saijo, M. Tanaka, H. Okawai, H. Sasaki, S.-I. Nitta, F. Dunn, Ultrasonic tissue characterization of infracted myocardium by scanning acoustic microscopy, Ultrasound Med. Biol. 23 (1) (1997) 77–85.
[2] Y. Saijo, H. Sasaki, H. Okawai, S.-I. Nitta, M. Tanaka, Acoustic properties of atherosclerosis of human aorta obtained with high-frequency ultrasound, Ultrasound Med. Biol. 24 (7) (1998) 1061–1064.

[3] Y. Saijo, C.S. Jørgensen, E. Falk, Ultrasonic tissue characterization of collagen in lipid-rich plaques in apoE-deficient mice, Atherosclerosis 158 (2001) 289–295.
[4] R.R. Cooper, S. Misol, Tendon and ligament insertion. A light and electron microscopic study, J. Bone Joint Surg. Am. 52A (1970) 1–20.
[5] H. Sano, Y. Saijo, S. Kokubun, Material properties of the supraspinatus tendon at its insertion-A measurement with the scanning acoustic microscopy, J. Musculoskeletal Res. 8 (1) (2004) 29–34.
[6] H. Sano, Y. Saijo, S. Kokubun, Non-mineralized fibrocartilage shows the lowest elastic modulus in the rabbit supraspinatus tendon insertion—measurement with scanning acoustic microscopy, J. Shoulder Elbow Surg., in press.
[7] N. Hozumi, R. Yamashita, C.-K. Lee, M. Nagao, K. Kobayashi, Y. Saijo, M. Tanaka, S. Ohtsuki, Time–frequency analysis for pulse driven ultrasonic microscopy for biological tissue characterization, Ultrasonics 42 (2004) 717–722.
[8] Y. Saijo, H. Sasaki, N. Hozumi, K. Kobayashi, M. Tanaka, T. Yambe, Sound speed scanning acoustic microscopy for biomedical applications, Technol. Health Care 13 (2005) 261–267.
[9] M. Benjamin, J.R. Ralphs, Fibrocartilage in tendons and ligament-an adaptation to compressive load, J. Anat. 193 (Pt 4) (1998) 481–494.
[10] H. Sasaki, Y. Saijo, M. Tanaka, H. Okawai, Y. Terasawa, T. Yambe, S.-I. Nitta, Influence of tissue preparation on the high-frequency acoustic properties of normal kidney tissue, Ultrasound Med. Biol. 22 (9) (1996) 1261–1265.
[11] K. Hasegawa, C.H. Turner, R.R. Recker, E. Wu, D.B. Burr, Elastic properties of osteoporotic bone measured by scanning acoustic microscopy, Bone 16 (1) (1995) 85–90.
[12] C.H. Turner, J. Rho, Y. Takano, T.Y. Tsui, G.M. Pharr, The elastic properties of trabecular and cortical bone tissues are similar: results from two microscopic measurement techniques, J. Biomech. 32 (1999) 437–441.
[13] T. Nomura, E. Gold, M.P. Powers, S. Shingaki, J.L. Katz, Micromechanics/structure relationship in the human mandible, Dental Mater. 19 (2003) 163–173.

Available online at www.sciencedirect.com
ScienceDirect
Ultrasonics 44 (2006) e51–e55
Ultrasonics
www.elsevier.com/locate/ultras

Ultrasonic speed microscopy for imaging of coronary artery

Yoshifumi Saijo [a,*], Naohiro Hozumi [b], Cheolkyou Lee [b], Masayuki Nagao [b], Kazuto Kobayashi [c], Nagaya Oakada [c], Naohiko Tanaka [d], Esmeraldo dos Santos Filho [a], Hidehiko Sasaki [a], Motonao Tanaka [a], Tomoyuki Yambe [a]

[a] *Department of Medical Engineering and Cardiology, Institute of Development, Aging and Cancer, Tohoku University, 4-1 Seiryomachi, Aoba-ku, Sendai 980-8575, Japan*
[b] *Department of Electrical Engineering, Toyohashi University of Technology, Toyohashi, Japan*
[c] *Honda Electronics Co. Ltd., Toyohashi, Japan*
[d] *Faculty of Systems Engineering, Shibaura Institute of Technology, Saitama, Japan*

Available online 3 July 2006

Abstract

We have been developing a scanning acoustic microscope (SAM) system for medicine and biology featuring quantitative measurement of ultrasonic speed and attenuation of soft tissues. In the present study, we will propose a new concept ultrasonic speed microscopy that can measure the thickness and ultrasonic speed using fast Fourier transform of a single pulsed wave instead of continuous waves used in conventional SAM systems. Six coronary arteries were frozen and sectioned approximately 10 μm in thickness. They were mounted on glass slides without cover slips. The scanning time of a frame with 300 × 300 pixels was 121 s and two-dimensional distribution of ultrasonic speed was obtained. The ultrasonic speed was 1720 m/s in the thickened intima with collagen fiber, 1520 m/s in lipid deposition underlying fibrous cap and 1830 m/s in calcified lesion in the intima. These basic measurements will help understanding echogenecity in intravascular ultrasound (IVUS) images. Imaging of coronary artery with the ultrasonic speed microscopy provides important information for study of IVUS coronary imaging.

Keywords: Acoustic microscopy; Ultrasonic speed; Coronary artery; Atherosclerosis

1. Introduction

Since 1985, we have been developing a scanning acoustic microscope (SAM) system for biomedical use and have been investigating the acoustic properties of various organs and disease states by using this SAM system [1–9]. In biomedicine, SAM is useful for intraoperative pathological examination, study of low-frequency ultrasonic images, and assessment of biomechanics at a microscopic level. The most important feature of our SAM system lies in providing quantitative values of ultrasonic speed and attenuation of thin slices of soft tissue.

In the present study, we will propose a new concept ultrasonic speed microscopy that can measure the thickness and ultrasonic speed using fast Fourier transform of a single pulsed wave instead of continuous waves used in conventional SAM systems. We measured the ultrasonic speed of the tissue components in coronary arteries and the results were compared with IVUS imaging of coronary artery in clinical settings.

2. Methods

2.1. Tissue preparation

Six human coronary artery specimens were involved in the present study. At the autopsy, the coronary arteries were frozen with OCT compounds, sectioned

* Corresponding author. Tel.: +81 22 717 8514; fax : +81 22 717 8518.
E-mail address: saijo@idac.tohoku.ac.jp (Y. Saijo).

0041-624X/$ - see front matter © 2006 Elsevier B.V. All rights reserved.
doi:10.1016/j.ultras.2006.06.050

approximately 10 μm in thickness to make a cross-sectional view of coronary artery and mounted on glass slides. The specimens were not stained or not covered with cover slips for ultrasonic speed microscopy observation.

2.2. Ultrasonic speed microscopy

Fig. 1 shows a block diagram of ultrasonic speed microscopy for biological tissue characterization. A single ultrasound pulse with a pulse width of 5 ns was emitted and received by the same transducer above the specimen. The aperture diameter of the transducer was 1.2 mm, and the focal length was 1.5 mm. The central frequency was 80 MHz, and the pulse repetition rate was 10 kHz. The diameter of the focal spot was estimated to be 20 μm at 80 MHz by taking into account the focal distance and sectional area of the transducer. Distilled water was used as the coupling medium between the transducer and the specimen. The reflections from the tissue surface and those from the interface between the tissue and glass were received by the transducer and were introduced into a digital oscilloscope (Tektronics TDS 5052, USA). The frequency range was 300 MHz, and the sampling rate was 2.5 GS/s. Four values of the time taken for a pulse response at the same point were averaged in the oscilloscope in order to reduce random noise.

The transducer was mounted on an X–Y stage with a microcomputer board that was driven by the computer installed in the digital oscilloscope through RS232C. The X-scan was driven by a linear servo motor, and the Y-scan was driven by a stepping motor. Finally, two-dimensional distributions of ultrasonic intensity, sound speed, and thickness of a specimen measuring 2.4 × 2.4 mm were visualized using 300 × 300 pixels. The total scanning time was 121 s.

2.3. Signal analysis [10]

The reflected waveforms are shown in Fig. 2. The waveform at the glass surface without the tissue is shown in (a). This signal was used as a reference waveform. The decline

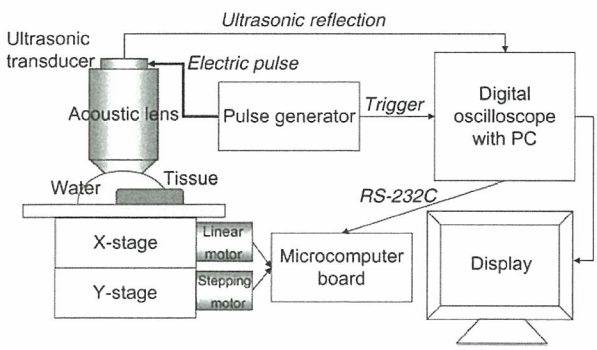

Fig. 1. Block diagram of ultrasonic speed microscopy developed with collaboration between Tohoku University, Toyohashi University of Technology and Honda Electronics Co. Ltd.

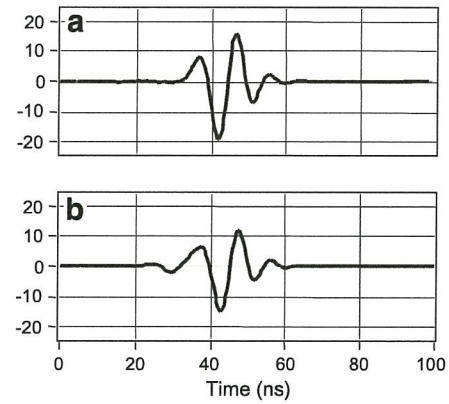

Fig. 2. Reflected waveforms (a) from the glass surface without tissue, and (b) from the tissue area.

of the glass surface was compensated by measuring three different points in the glass area surrounding the tissue. The waveform from the tissue area is shown in (b). Although the waveform contains two reflections at the surface and at the interface of the tissue and glass, the two components cannot be separated in time domain analysis. Thus, frequency domain analysis was performed by analyzing the interference between the two reflections. Intensity and phase spectra were calculated by Fourier transforming the waveform. The spectra were normalized by the reference waveform. Fig. 3 shows the frequency domain analysis of the interfered waveform.

Denoting the minimum point in the intensity spectrum by $f_{\min}$ and the corresponding phase angle by $\phi_{\min}$, the phase difference between the two reflections at the minimum point is $(2n-1)\pi$, which yields

$$2\pi f_{\min} \times \frac{2d}{c_0} = \phi_{\min} + (2n-1)\pi \tag{2}$$

where d, c_0, and n are the tissue thickness, sound speed of water, and a non-negative integer, respectively. Denoting

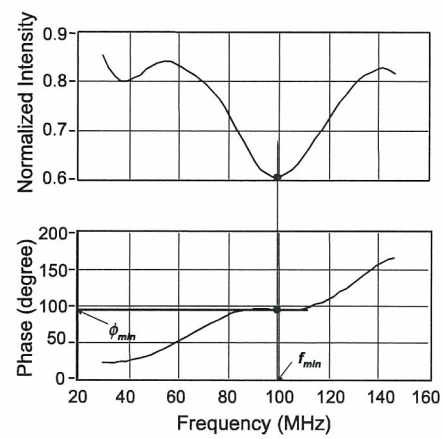

Fig. 3. Frequency domain analysis of interfered waveform. $f_{\min}$: the minimum point in the intensity spectrum, $\phi_{\min}$: corresponding phase angle.